ELSEVIER

Journal of Fluids and Structures 19 (2004) 651–668

JOURNAL OF FLUIDS AND STRUCTURES

www.elsevier.nl/locate/jnlabr/yjfls

Active twist rotor blade modelling using particle-wake aerodynamics and geometrically exact beam structural dynamics

C.E.S. Cesnik[a,*], D.G. Opoku[b], F. Nitzsche[b], T. Cheng[c]

[a] *Department of Aerospace Engineering, The University of Michigan, Ann Arbor, MI 48109-2140, USA*
[b] *Department of Mechanical and Aerospace Engineering, Carleton University, Ottawa, Ont., Canada K1S 5B6*
[c] *Department of Aeronautics and Astronautics, Massachusetts Institute of Technology, Cambridge, MA 02139-4307, USA*

Received 30 September 2003; accepted 26 January 2004

Abstract

An active aeroelastic and aeroacoustic analysis of helicopter rotor systems is presented in this paper. It is a tightly coupled computational aeroelastic code that interfaces a particle-wake panel method code with an active nonlinear mixed variational intrinsic beam element code. In addition, a Ffowcs-Williams–Hawkings equation-based acoustic component is incorporated to complete the numerical implementation. The theory behind each component is summarized here as well as the method for coupling the aerodynamic and structural components. Sample acoustic and aeroelastic results are given for different model-scale rotors. Comparisons with available (passive) results show very good agreement. Preliminary study with an active twist rotor is also shown.

1. Introduction

Although rotorcraft provide a means for completing unique missions due to their maneuverability, their use is currently restricted due to their substantial noise and vibration. The vibration and noise produces restrictions due to passenger and pilot comfort, fatigue, and effect on the surrounding environment.

In an effort to alleviate some of the limitations due to noise and vibration, the helicopter community has embarked on several research programs to understand the mechanisms that produce these disturbances and investigate methods to address them [e.g., Kube et al. (1994); Splettstoesser et al. (1993)]. One of the major causes of rotorcraft noise and vibration is the unsteady aerodynamic environment the rotor creates and aeroelastic interaction between the rotor blades and this environment.

With the introduction of smart materials, new noise and vibration control concepts have been recently pursued. Several notable smart material individual blade control (IBC) concepts have emerged, particularly trailing-edge flap and integral twist actuation. Trailing-edge flap actuation involves the use of smart materials to deflect a trailing edge flap at the outer portion of the blade [e.g., Prechtl and Hall (2000)]. Integral twist actuation uses layers of active piezocomposite material embedded in the blade to cause twist deformation along its length [e.g., Cesnik et al. (1999)]. Another interesting actuation mechanism that has been proposed in the literature is the smart-spring root actuation

*Corresponding author. Tel.: +1-734-764-3397.
E-mail addresses: cesnik@umich.edu (C.E.S. Cesnik), dopoku@engsoc.carleton.ca (D.G. Opoku), fred_nitzsche@carleton.ca (F. Nitzsche), taocheng@mit.edu (T. Cheng).

0889-9746/$ - see front matter
doi:10.1016/j.jfluidstructs.2004.01.007

that dynamically modifies the boundary condition at the root by changing its impedance [e.g., Zimcik et al. (2002)]. The common technique of all of these concepts is the use of smart materials to actively control each blade to alter its aeroelastic response to the surrounding unsteady aerodynamic environment in the rotating frame.

In support of this work, there is a need for rotorcraft analysis codes that are capable of accurately modelling the unsteady aerodynamic environment that the rotor blades are subject to and capturing the structural response of the rotor blades within a proper aeroelastic framework. In addition, the ideal code would have the capability to model smart material IBC concepts and have a component capable of providing acoustic results for noise reduction studies.

The broad objective of the current work is to develop an active aeroelastic aeroacoustic rotorcraft code to study noise and vibration. The aerodynamic component is a high-resolution unsteady panel method with a particle-wake model. Data from the aerodynamic component are used to obtain acoustic results. The structural component is a nonlinear beam element model of the rotor blades based on a mixed variational intrinsic formulation, which incorporates the effects of embedded piezoelectric actuators. Together, these components form a tightly coupled aeroelastic code in the time domain.

This paper focuses on the development of the aeroelastic aeroacoustic code, describing the aerodynamic and structural solvers and their coupling, as well as the acoustic component. Example acoustic results are presented for a model rotor with rigid blades. Aeroelastic results are presented for passive and active model rotors.

2. Aerodynamic component

Computational modelling of rotorcraft aerodynamics is a unique and challenging problem. To properly model a rotorcraft, the interaction between several bodies must be captured. In addition, the influence of the wake must be accounted for as it has strong influence on the aerodynamics of the rotor. These factors combine to make rotorcraft modelling a difficult and computationally expensive task. Accurate modelling of rotorcraft aerodynamics is essential for research and development in several disciplines. Structural dynamic and aeroelastic analysis of rotor blades requires an aerodynamic model capable of accurately predicting loads to determine the interaction between the structure and aerodynamics. Investigation of methods for active and passive control for vibration and noise reduction also requires accurate aerodynamic models to accurately predict the aeroelastic response.

Grid-based computational fluids dynamics (CFD) codes have been used with relative success to model rotorcraft aerodynamics [e.g., Strawn and Djomehri (2001); Beamier (2000); Pahlke and Chelli (2000)]. While CFD has the potential to eventually provide very detailed aerodynamic calculations, it often has difficulty in capturing wake effects. In addition, CFD is generally too computationally expensive to closely couple with analyses for studies such as aeroelasticity and aeroacoustics. An alternative approach is to use a panel method or lifting-line model coupled with a vortex-wake model for aerodynamic modelling (Ahmed and Vidjaja, 1994; Wachspress et al., 2000; Johnson, 1998). These methods have been shown to accurately model the aerodynamics of a rotor in a variety of flight situations with computational costs that are orders of magnitude less than CFD (Leishman, 2000).

The GENeral Unsteady Vortex Particle (GENUVP) code was developed at the National Technical University of Athens (NTUA) (Voutsinas, 1990; Voutsinas et al., 1995; Voutsinas and Triantos, 1999a). GENUVP is a panel method code with a vortex particle-wake model for calculating the flowfield around multi-component configurations. Through collaboration with NTUA, GENUVP was modified at Carleton University for use as the aerodynamic component of the present work.

The core theory of GENUVP is the use of the Helmholtz decomposition theorem through which the influence of solid bodies such as rotor blades, fuselage, and stabilizers is captured along with the influence of the wake.

Consider the unsteady flow of an incompressible and inviscid fluid around a multi-component configuration. The bodies are allowed to move independently, a necessary feature for helicopter configurations. Let $\mathbf{u}(\mathbf{x};t)$, $\mathbf{x}\in D$, $t\geqslant 0$ denotes the velocity of the fluid where D is the flowfield. Then according to the Helmholtz decomposition theorem, $\mathbf{u}$ can be split into two parts: irrotational and rotational. Usually the presence of solid boundaries is included in the irrotational part, $\mathbf{u}_{\text{solid}}$ whereas the wakes are included in the rotational part, $\mathbf{u}_{\text{wake}}$. Thus,

$$\mathbf{u}(\mathbf{x};t)=\mathbf{u}_{\text{ext}}(\mathbf{x};t)+\mathbf{u}_{\text{solid}}(\mathbf{x};t)+\mathbf{u}_{\text{wake}}(\mathbf{x};t), \tag{1}$$

where $\mathbf{u}_{\text{ext}}$ denotes a given external field possibly varying in space and time. Green's theorem provides the means to express $\mathbf{u}_{\text{solid}}$ through surface singularity distributions suggesting the use of a panel method in approximating this term. As for $\mathbf{u}_{\text{wake}}$, the Biot–Savart law gives,

$$\mathbf{u}_{\text{wake}}(\mathbf{x}_0;t)=\int_{D_\omega(t)}\frac{\boldsymbol{\omega}(\mathbf{x};t)\times(\mathbf{x}_0-\mathbf{x})}{4\pi|\mathbf{x}_0-\mathbf{x}|^3}\,\mathrm{d}D, \tag{2}$$

where $D_\omega(t)$ denotes the support of vorticity. From Eq. (2), the use of vortex methods (VMs) in approximating $\mathbf{u}_{\text{wake}}$ is derived. Accordingly, this (decomposition) Eq. (1) combines a panel method with VMs as a suitable numerical model. The two parts in Eq. (1) must be linked to each other through coupling conditions, which feed $\mathbf{u}_{\text{wake}}$ with vorticity continuously in time.

2.1. Panel method—$\mathbf{u}_{\text{solid}}$

Following Hess (1972), an indirect panel method is used for modelling solid bodies in GENUVP. In GENUVP, lifting bodies, i.e., the rotor blades or stabilizers, can be modelled as either thin or thick lifting bodies. Thin lifting bodies are modelled using dipole distributions and thick lifting bodies are modelled using a combination of dipole and source distributions. For the current work, thin lifting bodies were used for modelling the rotor blades. In GENUVP, trailing and tip edge wake strips are emitted at every time step—referred to as the near wake. Matching the strength of each wake element with the strength of the adjacent emitting dipole element (i.e., trailing or tip edge) on the blade enforces the zero pressure jump Kutta condition.

Nonlifting bodies can also be modelled in GENUVP using source distributions to model the body geometry. In this way, the effects of a fuselage on the rotor inflow can also be modelled.

2.2. Vortex particle methods—$\mathbf{u}_{\text{wake}}$

It is well established that the wake has a large influence on the aerodynamics of rotorcraft (Leishman, 2000). As such, an accurate wake model is essential for rotorcraft aerodynamic model. Following Rehbach (1973), a vortex blob approach was taken to model the far-field wake in GENUVP. With this approach, a cloud of vortex particles, each one associated with vector quantities, namely, intensity, velocity, and position, represents the wake. The evolution of the vortex particle wake is carried out using a Lagrangian description that accounts for the stretching of vorticity. Modelling of vortex stretching allows the vortex particle wake to capture the effects of wake deformation. The induced velocity due to each vortex particle is determined with a smoothed approximation of the Biot–Savart law given by Beale and Majda (1985).

2.3. Near to far-field coupling scheme

After the panel method calculations of a given time step, the near-wake strip elements are transformed into vortex particles and become part of the far wake. This is done by integrating the vorticity of each near-wake dipole element to form a vortex particle (Voutsinas, 1990). The new vortex particles become a part of the far wake, which evolves prior to the next time step. Refer to Fig. 1 for a schematic of the vortex blob generation process.

2.4. Reduction of computational cost

For code effectiveness, computational cost must be kept to a minimum. Two schemes were introduced into GENUVP to reduce the code's computational cost—subgrid and particle-mesh (PM) approximations (Voutsinas and Triantos, 1999a).

Subgrid approximations were implemented to help reduce the cost of the panel method calculations. As pointed out by Hess and Smith (1968), exact integral evaluations are necessary only when the distance between control point and the panel center is small. In fact, when the distance of the evaluation point from the panel gets larger than four times the maximum diagonal of the panel, the integral evaluation can be reduced to a point calculation. Reversing this result, one can expect that the error will also be small if distant panels are grouped into larger ones, over which the integrals are evaluated (Vassberg, 1997). A strategy to such a grouping has been extended to dipole distributions and implemented by introducing a sequence of paneling at different levels of refinement as shown in Fig. 2. Calculations start at the lowest level (coarse paneling). Depending on the distance between the panel center and the evaluation point, the calculations will either proceed with the integral evaluation over the large panel or pass to the next and more refined level of paneling. Consider a panel of surface S, which contains n panels of the highest level in which the unknown singularity X is defined. Let I_1 denote the value of the integral evaluated over S for unitary singularity strength. Then the collective contribution of the n panels is approximated by

$$I = \sum_{i=1}^{n} I_1 \frac{S_i}{S} X_i, \tag{3}$$

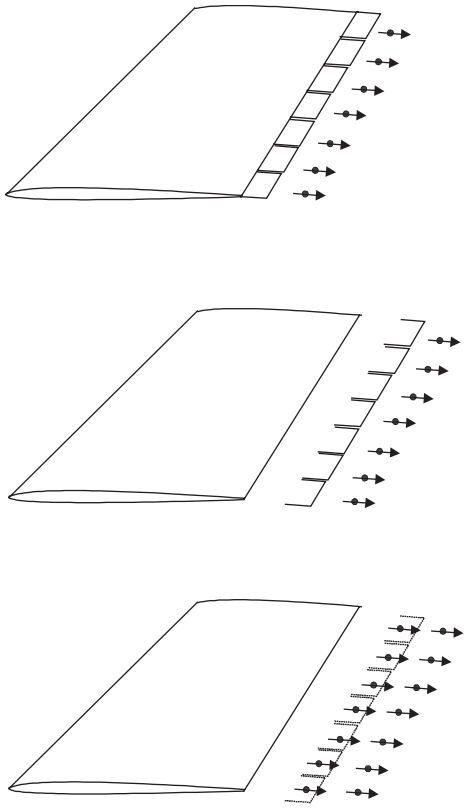

Fig. 1. Formation of vortex particles from a trailing-edge wake strip.

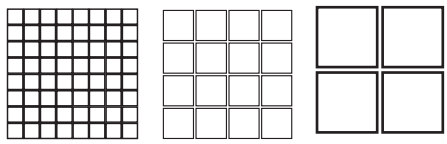

(a) The three levels of paneling

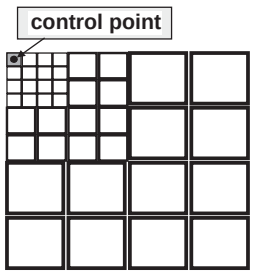

(b) The activation of the different levels

Fig. 2. Diagram of the grid refinement levels used for subgrid approximation.

where S_i denotes the surface area of the ith high-level panel. Depending on the number of unknowns, the final system is either solved directly or iteratively in which case the matrix need not be stored. Thus, paneling of the order of several thousands can be used on ordinary workstations.

Conventional vortex methods involve direct evaluation of the velocity and the deformation at every blob position based on the Biot–Savart law. This means that for N vortex blobs a complete time step requires N^2 point-to-point calculations. As the simulation proceeds, N increases continuously in time, as does the computational cost, becoming prohibitive at large times. One way of managing cost is to use PM techniques (Hockney and Eastwood, 1981), which reduces the cost from N^2 to $N \cdot \log(N)$ calculations per time step. The concept is simple: for a large number of blobs, $\mathbf{u}$ and its spatial derivatives that define the deformation tensor $\mathbf{D}$, are evaluated at the nodes of a Cartesian grid containing $D_\omega(t)$. Then, local interpolation is used to determine $\mathbf{u}$ and $\mathbf{D}$ at the exact positions of the blobs. To this end, the vector potential $\mathbf{A}$ of $\mathbf{u}_{\text{wake}}$ is introduced:

$$\nabla \times \mathbf{u}_{\text{wake}} = \mathbf{A}; \tag{4}$$

and the corresponding Poisson equation

$$\nabla^2 \mathbf{A} = -\boldsymbol{\omega}, \text{ in } D_\omega(t) \tag{5}$$

is solved by means of the Fourier method. This choice was made in order to keep the cost to a minimum.

More specifically at every time step the PM calculation procedure involves a projection step, a solution step, and an interpolation step. In the projection step, vorticity is evaluated over a Cartesian mesh that includes all vortex blobs, by projecting the intensity of the vortex blobs located within a cell of the mesh onto the vertices of the cell. In the solution step, Eq. (5) is discretized using central differences. Three heptadiagonal linear systems are obtained. The values of $\mathbf{A}$ at the boundary nodes of the grid are provided by point-to-point Biot–Savart calculations. A Fourier method is then used to solve the linear systems for the nodal values of the velocity potential $\mathbf{A}$. Once the nodal values of the vector potential are obtained, standard central differences are used to evaluate the velocity and the deformation at the nodes of the grid. Finally, the velocity and the deformation of vorticity of each vortex blob are calculated by interpolation from the nodal values of the nearby grid nodes.

Accuracy in PM methods is restricted by the grid cell size. In order to reduce the error of PM schemes, local corrections proposed by Anderson (1986) are introduced. Experience has shown that even corrected PM schemes are not sufficiently accurate and, therefore, they should not be applied to areas of major importance. In GENUVP a mixed scheme was followed which excludes areas close to solid boundaries from PM calculations. For example, in the case of a helicopter in forward flight, the PM region would start downstream of the tail rotor and extends to infinity.

Through a combination of subgrid and PM approximations, the computational cost in GENUVP can be kept manageable. GENUVP has the capability to model full rotorcraft configurations, including the main and tail rotors, fuselage, and stabilizers.

3. Structural component

For the structural representation of the active blade, a geometrically exact formulation for the dynamics of moving beams is used. For that, an asymptotic analysis takes the electromechanical three-dimensional problem and reduces it to a set of two analyses: a linear analysis over the cross-section and a nonlinear analysis of the resulting beam reference line. The nonlinear 1-D global analysis considering small strains, finite rotations, and effects of embedded piezocomposite actuators used herein was presented by Cesnik et al. (2001) and it is based on the mixed variational intrinsic formulation for dynamics of moving beams originally presented by Hodges (1990) and Shang (1995). These equations are solved here in time domain, and details of its development can be found in Cheng (2002).

3.1. Mixed formulation for dynamics of moving beams with embedded piezocomposite actuators

The notation used in the present paper is based on matrix notation and is consistent with the original work of Hodges (1990) and Cesnik and Shin (2001). Some steps of the original work are repeated here to help understanding the mixed variational intrinsic formulation for dynamics of moving beams with anisotropic piezocomposite actuators. The three frames that are used by the mixed formulation for dynamics of moving beams are shown in Fig. 3. The global frame named a with its axes labeled a_1, a_2 and a_3 is rotating with the rotor at angular velocity Ω. The undeformed blade reference frame is named b, with its axes labeled b_1, b_2 and b_3, and the deformed blade reference frame is named B with its axes labeled B_1, B_2 and B_3. Using transformation matrices, any arbitrary vector U represented by its components in one frame may be converted into another. For example, $U_B = C^{Ba} U_a$ or $U_b = C^{ba} U_a$, where C^{Ba} is the transformation matrix from frame a to frame B, and C^{ba} is that from frame a to frame b. C^{Ba} contains unknown rotation variables, while C^{ba} is known and can be expressed in terms of direction cosines from the geometry of the undeformed rotor blade.

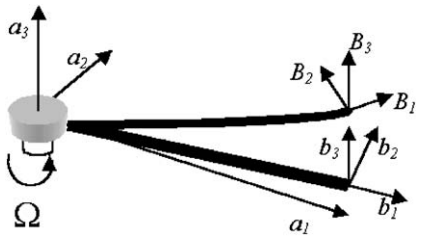

Fig. 3. Diagram showing the global reference frame a, undeformed beam reference frame b and deformed beam reference frame B.

The mixed variational formulation is derived using Hamilton's principle and can be written as

$$\int_{t_1}^{t_2}\int_0^l \left[\delta(K-U)+\overline{\delta W}\right]\,\mathrm{d}x_1\mathrm{d}t = \overline{\delta A}, \tag{6}$$

where t_1 and t_2 are arbitrarily fixed times, l is the length of the beam, K and U are the kinetic and potential energy densities per unit length, respectively. $\overline{\delta A}$ is the virtual action at the ends of the beam and at the ends of the time interval, and $\overline{\delta W}$ is the virtual work of applied loads per unit length.

The variation of the kinetic energy terms is with respect to the linear velocity column vector V_B and angular velocity column vector Ω_B, respectively. The velocities are all measured in the deformed blade frame B. The variation of the potential energy terms is with respect to the generalized strain column vectors γ and κ. The force and moment strain vectors γ and κ are also measured in the deformed blade frame B. F_B and M_B are the internal force and moment column vectors and P_B and H_B are the linear and angular momenta column vectors, defined as

$$F_B=\left(\frac{\partial U}{\partial \gamma}\right)^{\mathrm{T}},\ M_B=\left(\frac{\partial U}{\partial \kappa}\right)^{\mathrm{T}},\ P_B=\left(\frac{\partial K}{\partial V_B}\right)^{\mathrm{T}},\ H_B=\left(\frac{\partial K}{\partial \Omega_B}\right)^{\mathrm{T}}. \tag{7}$$

The subscripts in the above equations indicate the frame of reference. The first element of F_B is the axial force and the second and third elements are shear forces in the deformed frame B. Similarly, the first element of M_B is the twisting moment and the second and third elements are bending moments.

The generalized strain and force measures and velocity and momenta measures are related through the constitutive relations in the following manner:

$$\begin{Bmatrix} F_B \\ M_B \end{Bmatrix} = [K]\begin{Bmatrix} \gamma \\ \kappa \end{Bmatrix} - \begin{Bmatrix} F_B^{(a)} \\ M_B^{(a)} \end{Bmatrix},\quad \begin{Bmatrix} P_B \\ H_B \end{Bmatrix} = [M]\begin{Bmatrix} V_B \\ \Omega_B \end{Bmatrix},$$

where $F_B^{(a)}$and $M_B^{(a)}$ are actuation forces and moments which depend on the geometry, material distribution, and applied electric field. The stiffness matrix $[K]$ is, in general, a 6×6 matrix, depending on material distribution and cross-sectional geometry. Detailed expressions for the stiffness and mass matrices and actuation vector are defined in Cesnik and Shin (2001).

The geometrically exact kinematical relations, as defined in Shang (1995), are given by

$$\gamma = C^{Ba}(C^{ba}e_1+u_a')-e_1,\quad \kappa = C^{ba}\left(\frac{\Delta-\frac{\tilde{\theta}}{2}}{1+\frac{\theta^T\theta}{4}}\right)\theta', \tag{9}$$

$$V_B = C^{Ba}(v_a+\dot{u}_a+\tilde{\omega}_a u_a),\quad \Omega_B = C^{ba}\left(\frac{\Delta-\frac{\tilde{\theta}}{2}}{1+\frac{\theta^T\theta}{4}}\right)\dot{\theta}+C^{Ba}\omega_a, \tag{10}$$

where u_a is the displacement vector measured in the a frame, θ is the rotation vector expressed in terms of Rodrigues parameters. The Rodrigues parameters are defined in terms of a rotation of magnitude about a unit vector, $\boldsymbol{e}=e_i\boldsymbol{b}_i$, as

$\theta_i = 2e_i \tan(\alpha/2)$. Δ is the 3×3 identity matrix, v_a and w_a are the initial velocity and initial angular velocity of a generic point on the a frame, and e_1 is the unit vector $[1, 0, 0]^T$. $\dot{u}_a$ and $\dot{\theta}$ are the time derivatives of displacement and rotation. u'_a and θ' are the derivatives with respect to the spanwise curvilinear coordinate. The rotation matrix, $C=C^{ab}C^{Ba}$ is expressed in terms of the rotation parameter, θ, as follows:

$$C = \frac{\left(1 - \dfrac{\theta^T\theta}{4}\right)\Delta - \tilde{\theta} + \dfrac{\theta\theta^T}{2}}{1 + \dfrac{\theta^T\theta}{4}},$$

where the $\tilde{\theta}$ operator converts θ to its dual matrix (Hodges, 1990).

To form a mixed formulation, Lagrange multipliers are used to enforce the satisfaction of the kinematical equations. Using the rotation matrix C, some transformations can be performed so that all δ quantities, displacement and rotation, are measured in the global frame a and the strains, velocities, forces and momenta are measured in the deformed blade reference frame, B. The a frame version of the variational formulation, based on exact intrinsic equations for dynamics of moving beams, was derived by Shang (1995).

3.2. Finite element discretization

Adopting the finite element method, the spatial domain of the blade is discretized into N elements. Hence, the resulting total potential is written as

$$\int_{t_1}^{t_2} \sum_{i=1}^{N} \delta\Pi_i \, \mathrm{d}t = 0, \tag{11}$$

where the index i indicates a general element with length $\mathrm{d}l$. Due to the formulation's weakest form, the simplest shape functions can be used (Shang, 1995). Once the discretization is applied, a set of partial differential equations in time can be written. In matrix notation,

$$F_S(X, \dot{X}) - F_L = 0, \tag{12}$$

where F_S is the structural operator, F_L is the load operator, and X is the unknown vector consisting of structural variables. In these equations, the actuation forces and moments, $F_B^{(a)}$ and $M_B^{(a)}$, are time dependent input parameters associated with F_S. The components of the unknown structural variables in X depend on the boundary condition. For a hingeless rotor blade, X is as follows:

$$X = [\hat{F}_1^T \; \hat{M}_1^T \; u_1^T \; \theta_1^T \; F_1^T \; M_1^T \; P_1^T \; H_1^T \cdots u_N^T \; \theta_N^T \; F_N^T \; M_N^T \; P_N^T \; H_N^T \; \hat{u}_{N+1}^T \; \hat{\theta}_{N+1}^T]^T, \tag{13a}$$

and for an articulated blade, there are some modifications of the unknown vector because of the hinges. Specifically, the two internal bending moments at the root of the articulated blade are zeros. However, the two bending rotation angles at the root are not zeros any more and become unknown variables. Therefore, the unknown vector $\hat{M}_1$ is modified as following:

$$\hat{M}_1^T = \begin{bmatrix} \hat{M}_{11} & \hat{\theta}_{12} & \hat{\theta}_{13} \end{bmatrix}, \tag{13b}$$

where $\hat{M}_{11}$ is the twisting moment at the root of the blade and $\hat{\theta}_{12}$, $\hat{\theta}_{13}$ are the lead-lag and flap rotations at the root in terms of Rodrigues parameters, respectively. Consequently, the two internal bending moments $\hat{M}_{12}$ and $\hat{M}_{13}$ are zeros, yielding free rotation at the articulation hinge.

3.3. Time integration

To integrate Eq. (12) in time, a second-order backward Euler method is used. The following finite difference discretization scheme is applied at each time step, n:

$$\dot{P}_i^n = \frac{3P_i^n - 4P_i^{n-1} + P_i^{n-2}}{2\Delta t},$$

$$\dot{H}_i^n = \frac{3H_i^n - 4H_i^{n-1} + H_i^{n-2}}{2\Delta t},$$

$$\dot{u}_i^n = \frac{3u_i^n - 4u_i^{n-1} + u_i^{n-2}}{2\Delta t}, \tag{14}$$

$$\dot{\theta}_i^n = \frac{3\theta_i^n - 4\theta_i^{n-1} + \theta_i^{n-2}}{2\Delta t},$$

where Δt is the time-step size. Superscripts indicate the time step and subscripts indicate the node number.

Writing Eq. (12) at time step n and using Eq. (14), a set of nonlinear algebraic equations is obtained

$$F_S(X^n) - F_L = 0, \tag{15}$$

where X^n is the unknown structural vector at time step n.

Newton's method is used to solve the nonlinear algebraic equations given by Eq. (15). The Jacobian matrix can be derived explicitly by differentiation:

$$[J] = \left[\frac{\partial Fs}{\partial X}\right], \tag{16}$$

whose expressions are listed in Shin (2001).

The solution of Eq. (15) describes the displacement, stress, and strain fields at each time step.

4. Acoustic component

Regarding rotorcraft aeroacoustic modelling, the most widely used formulation is based on the Ffowcs-Williams–Hawkings (FW–H) equation (Ffowcs-Williams and Hawkings, 1969).

Let $\boldsymbol{x}$ and $\boldsymbol{y}$ be the observer and source position vectors, respectively, and $f(\boldsymbol{y},t) = 0$ describe the motion of the surface of a body. The FW–H equation that gives the sound generated by the body moving through a fluid is given by

$$\left(\frac{1}{c^2}\frac{\partial^2}{\partial t^2} - \nabla^2\right)p' = \frac{\partial}{\partial t}\left[\rho_o v_n |\nabla f|\delta(f)\right] - \frac{\partial}{\partial x_i}\left[l_i |\nabla f|\delta(f)\right] + \frac{\partial^2}{\partial x_i \partial x_j}\left[T_{ij}H(f)\right], \tag{17}$$

where p' is the acoustic pressure at the observer position, c and ρ_o are the speed of sound and the density of the undisturbed medium, respectively, $v_n = v_i n_i$ is the local normal velocity on the body surface (n_i is the body local outward normal), l_i is the local force on the fluid per unit area, and T_{ij} is the Lighthill stress tensor. $\delta(f)$ and $H(f)$ are the Dirac delta and Heaviside function, respectively. The three terms on the right-hand side of Eq. (17) are the thickness, loading, and quadrupole noise sources, respectively. The thickness noise source accounts for noise due to the displacement of the fluid by the finite thickness of the body. The loading noise source accounts for noise due to loading and change of loading on the body. The noise due to compressibility effects is included in the quadrupole noise source. For the current work, the quadrupole noise source is not considered, as it is a volume source that requires a grid-based flow solver.

Voutsinas and Triantos (1999b) previously introduced a solution of the FW–H equation into GENUVP for thickness and loading noise given by Farassat and Succi (1980). This solution discretizes the body into elements, each with associated volume and loading. Each element is a source of thickness and loading noise. Voutsinas and Triantos (1999b) were successful in implementing this solution into GENUVP and validating their results against the HELINOISE and HART experiments. In the current work, a new acoustic formulation based on Farassat's 1A solution of the FW–H equation (Farassat and Succi, 1983) is added to GENUVP. The 1A formulation is a solution of the FW–H equation for thickness and loading noise by integration over the body surface. The derivation of the 1A formulation can be found in Farassat and Succi (1983), therefore only the final solution is repeated here:

$$4\pi p'_L(\boldsymbol{x},t) = \frac{1}{c}\int_{f=0}\left[\frac{\dot{l}_i \hat{r}_i}{r(1-M_r)^2}\right]_{\text{ret}} \mathrm{d}S + \int_{f=0}\left[\frac{l_r - l_i M_i}{r^2(1-M_r)^2}\right]_{\text{ret}} \mathrm{d}S + \frac{1}{c}\int_{f=0}\left[\frac{l_r(r\dot{M}_i\hat{r}_i + cM_r - cM^2)}{r^2(1-M_r)^3}\right] \mathrm{d}S, \tag{18}$$

$$4\pi p'_T(\boldsymbol{x},t) = \frac{1}{c}\int_{f=0}\left[\frac{\rho_o v_n(r\dot{M}_i\hat{r}_i + cM_r - cM^2)}{r^2(1-M_r)^3}\right]_{\text{ret}} \mathrm{d}S,$$

$$p'(\boldsymbol{x},t) = p'_L(x,t) + p'_T(x,t),$$

where $\boldsymbol{r} = \boldsymbol{x}-\boldsymbol{y}$, $M_i = v_i/c$, $M_r = M_i\, r_i/r$, and $l_r = l_i\, r_i/r$. Eq. (18) gives the loading (p'_L), thickness (p'_T), and total (p') acoustic pressures at $\boldsymbol{x}$, respectively. The loading and thickness noise terms are calculated from the aerodynamic data. As before, the lifting surface of the blades is discretized into panel elements, each of which is an acoustic source. The

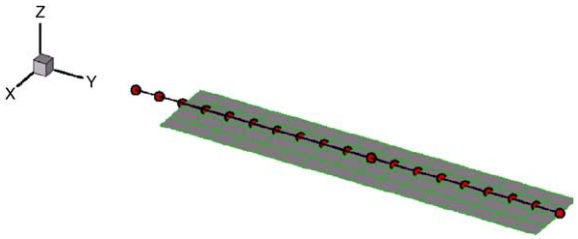

Fig. 4. Visualization of the structural and aerodynamic mesh for a single rotor blade.

loading noise is calculated from the loading and velocity of each element. Special consideration is needed for the thickness noise term since thin lifting bodies are used in the current work and the thickness noise term is dependent on v_n, the local normal velocity on the actual blade surface. To calculate v_n on the actual blade surface, the velocity on the thin surface is used together with the known geometry of the airfoil section. The loading and thickness noise contributions of all elements are summed to obtain the total acoustic noise signal. It should be noted that a time sequencing scheme is used in this summation process to account for the difference in travel time to the microphone for each acoustic emission.

5. Aeroelastic coupling

The aerodynamic and structural components maintain separate representations of the rotor blades. Fig. 4. shows the representation of a single blade for each component. The structural component is a 1D beam element discretization of the beam reference axis from the hub attachment point to the tip. The mean surface of the lifting portion of the blade is discretized in fine panels that constitute the aerodynamic mesh. The meshes are spanwise coincident over the length of the lifting surface. That is, for every structural beam element there is a corresponding aerodynamic strip of panel elements. This approach was taken to avoid the need for data interpolation at different spanwise stations.

The aeroelastic coupling between the aerodynamic and structural components is based on an extension of the classic 2-D airfoil section aeroelastic problem. A basic 2-D airfoil section aeroelastic system is shown in Fig. 5. This system is a simplified representation of the aeroelastic coupling method. The section has plunge, lag, and pitch degrees of freedom, with elastic springs restraining the motion along in each degree of freedom. The effective section elasticity and loading are modelled by the structural and aerodynamic components, respectively. Offset between the beam reference axis and aerodynamic center is considered. This system is extended to 3-D in the following manner. At every spanwise section, loading is computed by the aerodynamic component, including the effect of elastic velocity and torsional rotation about the beam reference axis. Although the structural component has six degrees of freedom at each spanwise node, three displacements and three rotations, only the plunge (flap), lag, extension, and pitch degrees of freedom are considered for the aeroelastic coupling.

Fig. 6 gives an overview of the coupling of components to form the combined code. It is a tightly coupled aeroelastic code that solves for a periodic solution in the time domain. At each timestep, aeroelastic data are exchanged between the aerodynamic component and structural component as illustrated in Fig. 7. The aerodynamic component solves for an effective angle of attack at every spanwise station. While lift and moment loads come directly from the aerodynamic calculations, the drag forces are estimated using 2-D airfoil lookup tables for the determined angles of attack. These loads are then sent to the structural component. The structural component then solves for elastic deformation (displacements and rotations) and rigid body motion (flapping and lead lagging). The elastic deformation and rate of elastic deformation are used to deform the aerodynamic mesh of the blades and alter the non-penetration boundary condition, respectively. The rigid body motion is used for rigid body velocity in the case of an articulated rotor.

6. Results

In the following sections, sample acoustic and aeroelastic results are presented. The acoustic results reflect the initial testing of the acoustic component prior to full integration in the new code developed here. For acoustic testing, a UH-1 H scale rotor is modelled. Aeroelastic testing models the BO-105 and the NASA/Army/MIT Active Twist Rotor (ATR) model systems.

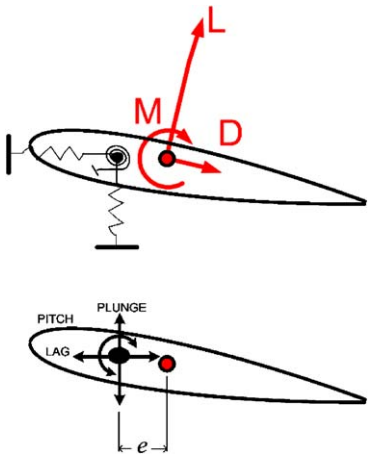

Fig. 5. Schematic diagram of the 2-D basis for aeroelastic coupling of the aerodynamic and structural components.

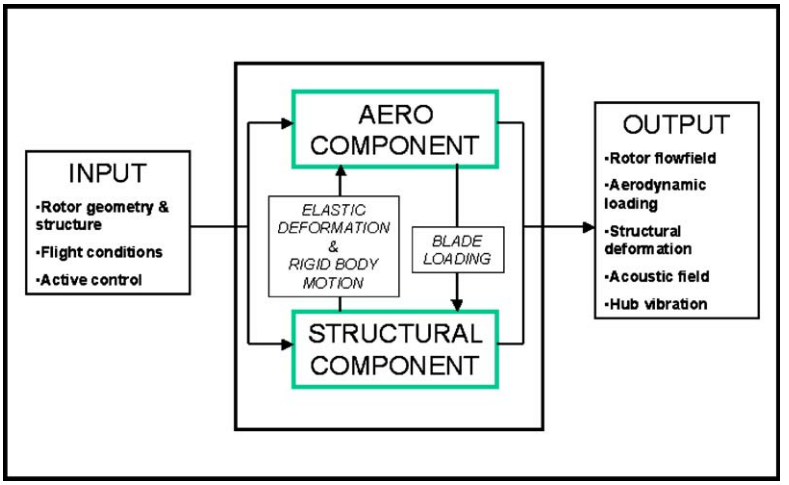

Fig. 6. An overview block diagram of current aeroelastic aeroacoustic formulation.

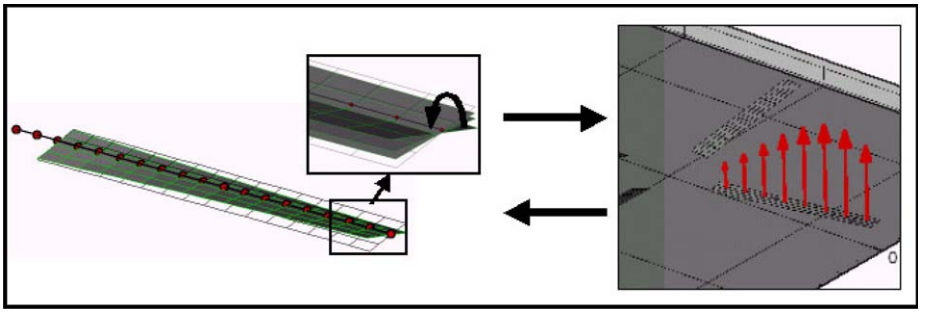

Fig. 7. An illustration of the exchange of data between the aerodynamic and structural components.

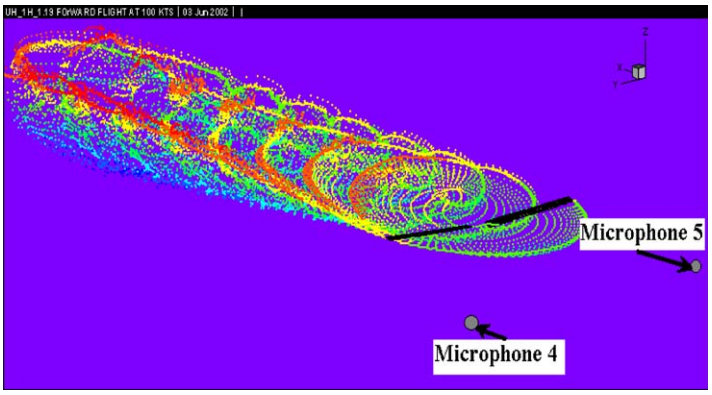

Fig. 8. Visualization of the wake produced by the UH-1 H rotor in forward flight and microphone locations.

6.1. Acoustic results

A UH-1 H rotor was used to validate the new acoustic formulation developed for the new aeroelastic aeroacoustic code. Details of the UH-1 H rotor are given in Conner and Hoad (1982). Results within this section were obtained using a rigid blade representation and, therefore, not using the (active) elastic structural component.

Fig. 8 shows a visualization of the particle wake produced by the UH-1 H rotor in forward flight ($\mu = 0.208$, 8.85° forward disc tilt) and the locations of two microphones where acoustic pressure is compared. Microphone 4 is 4 m ahead of the rotor hub on the advancing side; microphone 5 is 4 m ahead of the rotor hub on the retreating side. Figs. 9 and 10 show a comparison of total acoustic pressure at the two microphone locations. Comparison is made with both WOPWOP (Brentner, 1986) and experimental (Conner and Hoad, 1982) data on the advancing side, and with experimental data on the retreating side. In both cases, the overall trend is captured. The higher frequency component present in the experimental results is not captured by either code. While some of this high-frequency component may be due to "experimental noise," it is suspected that some of the oscillation may be due to flexibility of the blades. Figs. 11 and 12 show comparisons of sound pressure level (SPL) versus frequency for the microphone on the advancing side of the rotor. The peaks in SPL at harmonics of the blade passage frequency are accurately captured.

6.2. Basic aeroelastic vibratory results

For a basic test of the aeroelastic prediction capability of the new code, the BO-105 model-scale rotor used in the HELINOISE experiment (Splettstoesser et al., 1993) is considered here. Detailed rotor properties can be found in Splettstoesser et al. (1993). Among the different test cases studied in the HELINOISE experiment, Table 1 shows the ones considered in this paper.

The vibratory load transferred to the hub can be calculated by adding the structural forces at the root boundary of the rotor blades. This gives an approximate measure of the vibration that the rotor would transfer to the fuselage. This result is approximate only because the inertia of the hub is not considered. However, it is a useful measure for vibration control study purposes.

Fig. 13 shows predicted vertical vibratory load amplitudes at harmonics of the rotor frequency. The results of the present analysis are evaluated as a comparison between different flight conditions. Constant "perceived" levels of vibration have the form of vibration amplitude decreasing asymptotically as a function of frequency, i.e., the same amplitude of vibration would be perceived as worse at a higher frequency. Considering this, relative to the other cases, case 1333 (descent) has the highest predicted vibratory load, with large oscillation amplitudes at 3P, 4P, and 8P. Case 344 (level flight) is also predicted to have a relatively high vibration, with large oscillation amplitudes at 4P and 8P. These results primarily reflect the structural response of the blades to the aerodynamic forcing due to interaction with the wake.

Fig. 14 is a visualization of the undeformed and deformed aerodynamic mesh of the BO-105 model for HELINOISE case 947. The deformation follows what would be expected for a hingeless rotor: zero deformation at the root and an upwards flap deformation increasing nonlinearly in the outward radial direction.

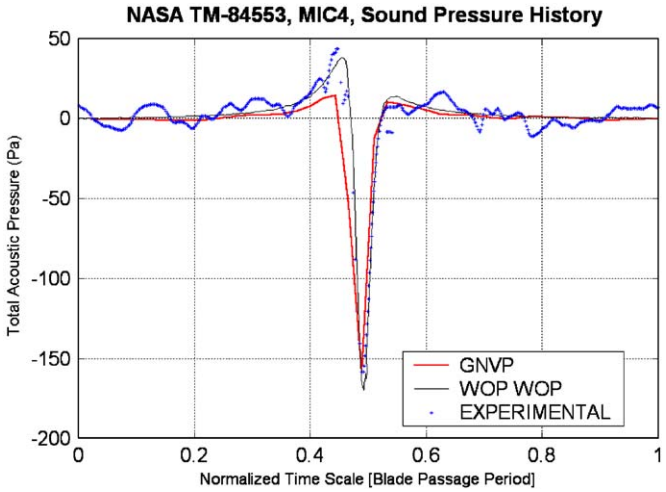

Fig. 9. Comparison of total acoustic pressure (advancing side microphone) for the UH-1 H in forward flight.

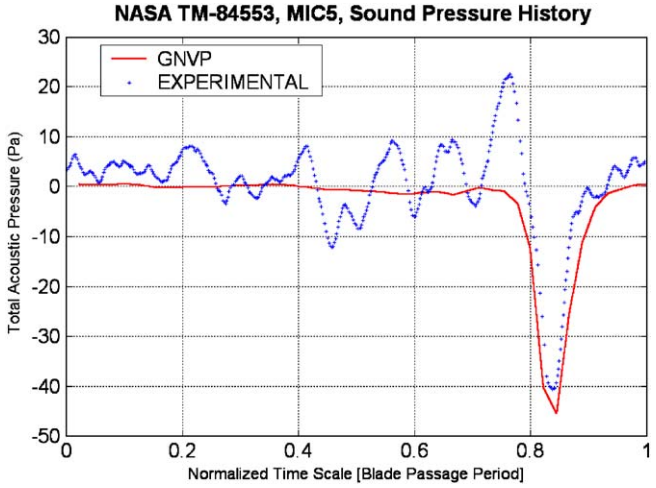

Fig. 10. Total acoustic pressure (retreating side microphone) for the UH-1 H in forward flight.

6.3. *Active aeroelastic results*

In order to numerically evaluate the aeroelastic modelling described in this paper, the time and frequency response of the ATR prototype blade in hover is presented. The passive and active properties of the blade are described in Shin (2001). Fig. 15 summarizes the geometric and material characteristics of the blade. Note that the active piezocomposite used in this blade is the active fiber composite (AFC) as described in Bent and Hagood (1997). For all the cases, the rotating speed of this rotor is 688 r.p.m and the collective pitch angle is 8°. The medium density is 2.432 kg/m^3 (heavy gas). There is a –10° built-in pretwist from the root to the blade tip. The root offset of the blade is 0.0762 m. A lead-lag damper was modelled with a damping coefficient of 10 Nm/(rad/s).

6.3.1. *ATR prototype blade in hover*

The aeroelastic solution of the rotating blades is separated into two steps: one is the steady analysis of the rotating blade in vacuum; the other is the dynamic analysis of the blade in gas. The deformations, internal forces and moments, and momenta of a rotating blade in vacuum are obtained by the steady state analysis. They are used in the dynamic analysis, with aerodynamic loads, as the initial rotating condition input. In the dynamic analysis, the blades are rotating

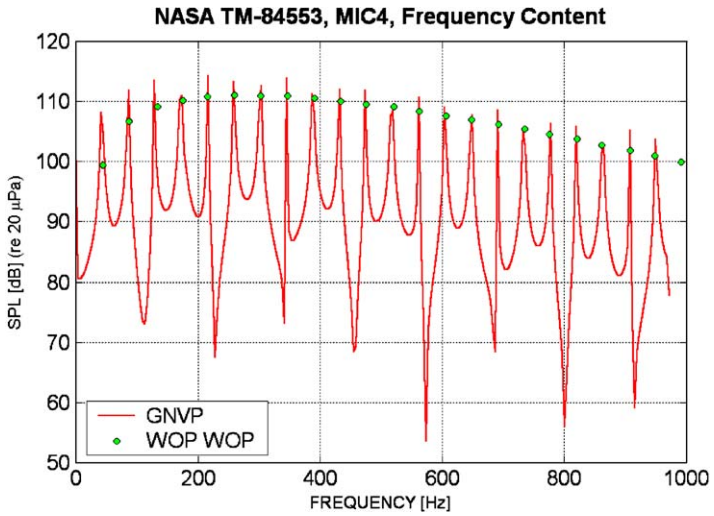

Fig. 11. Comparison (versus WOP WOP) of frequency content of the total acoustic pressure prediction of the advancing side microphone—UH-1 H in forward flight.

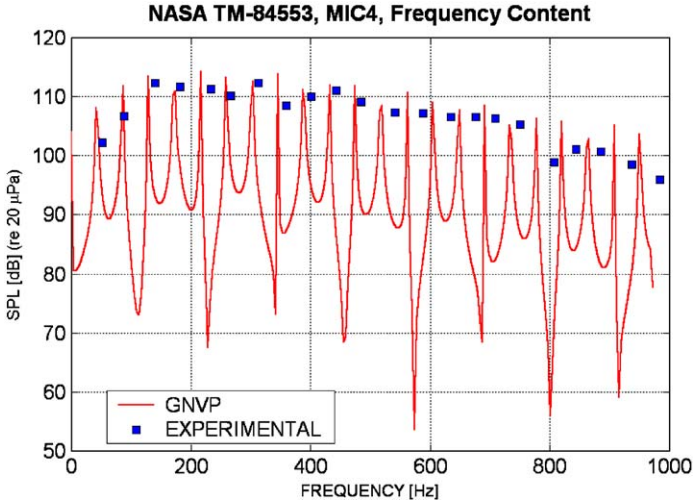

Fig. 12. Comparison (versus experimental data) of frequency content of the total acoustic pressure prediction of the advancing side microphone—UH-1 H in forward flight.

Table 1
Selected low-speed HELINOISE test cases (Splettstoesser et al., 1993)

Helinoise test case no.	Description
947	Near hover
344	Low-speed level flight (0.15 advance ratio)
508	Low-speed climb (0.15 advance ratio, 12° flight path angle)
1333	Low-speed descent (0.15 advance ratio, −6° flight path angle)

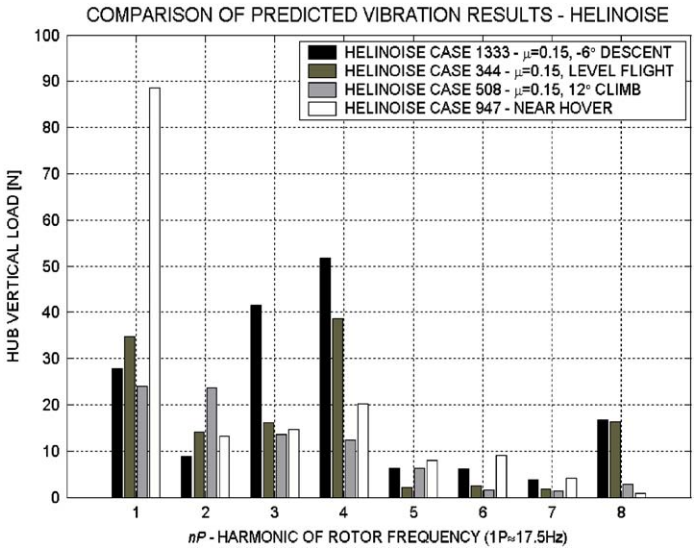

Fig. 13. A comparison of the present predicted vertical vibratory loads transferred to the hub for different HELINOISE test cases.

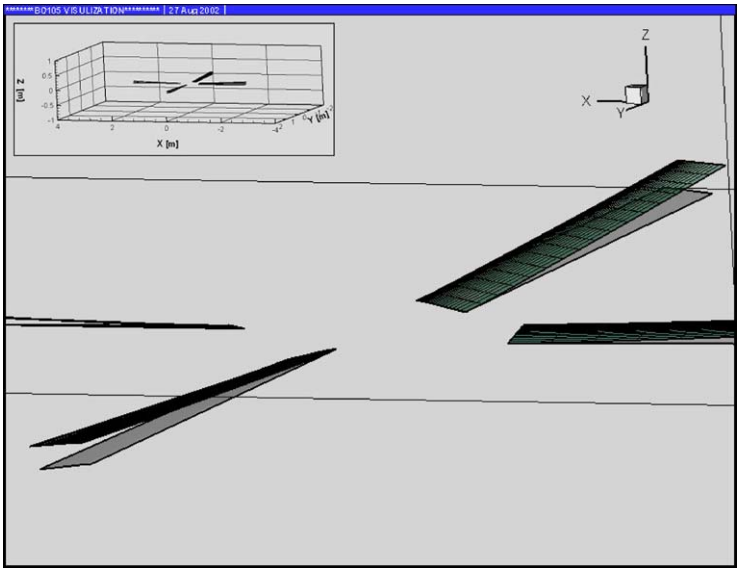

Fig. 14. A visualization of the undeformed (gray) and deformed (translucent black mesh) aerodynamic mesh of the BO105 rotor for HELINOISE case 947.

at their full speed at the first structural time step. However, in the aerodynamic module, the rotating speed is increased from zero to the full speed gradually in order to avoid suddenly applied aerodynamic forces, which result in large numerical blade oscillations. In this case, the time for the rotating speed to reach full speed is 1.0 s. Fig. 16 shows the developed wake of vortex particles in hover.

6.3.2. *Actuation test of ATR prototype blade in hover*

In this test case, the actuation is a sine-sweep signal ranging from 0 to 100 Hz as shown in Fig. 17. This actuation twist moment is applied after the full rotating speed is reached. The time step size used for the time integration in this case is 10^{-3} s. The corresponding tip twist response in trim is shown in Fig. 18. The frequency response obtained by the

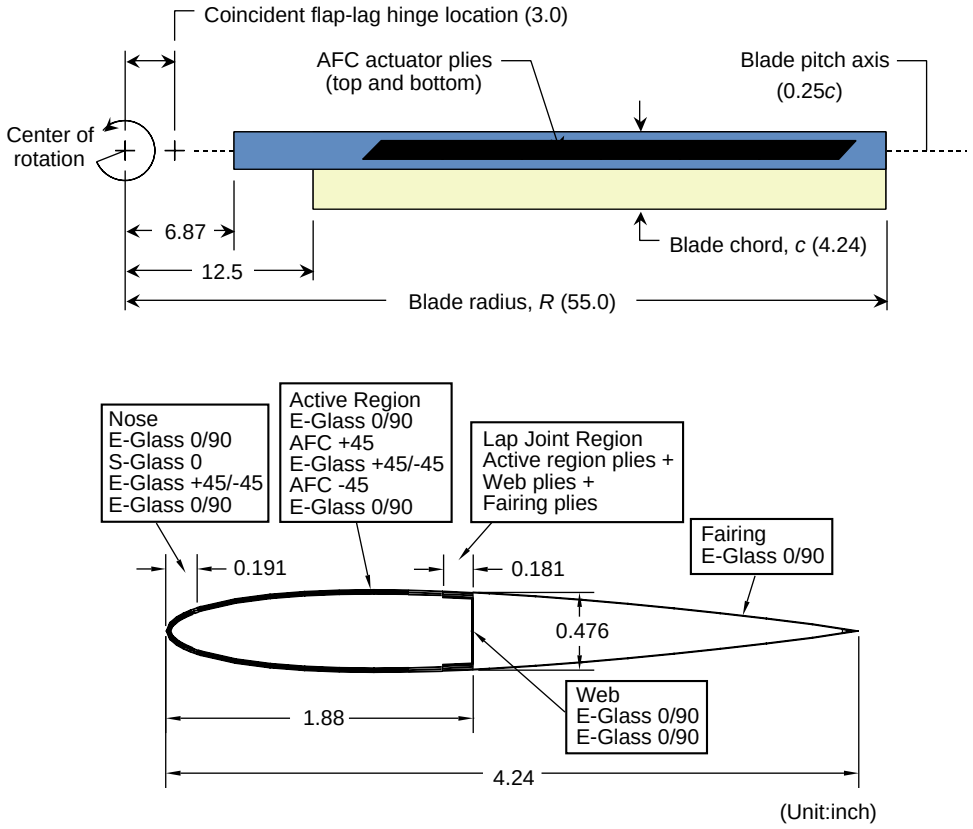

Fig. 15. Planform and cross-section of the ATR prototype blade.

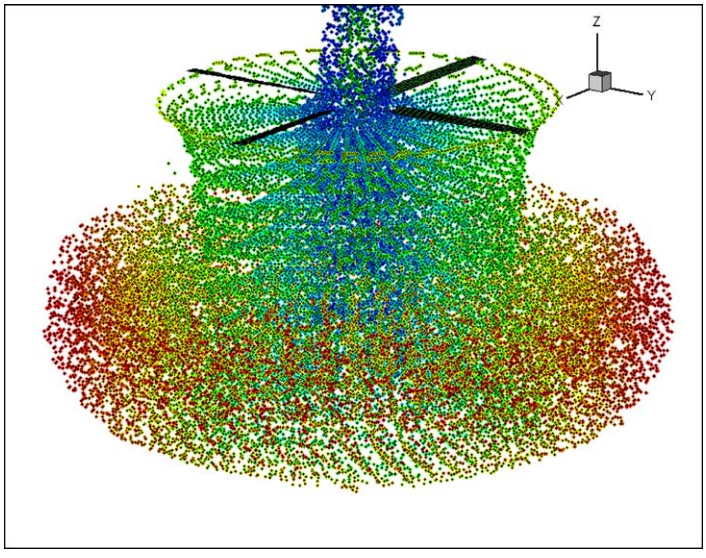

Fig. 16. Wake particle vortex development for the ATR system in hover (688 r.p.m, heavy gas, 8° collective).

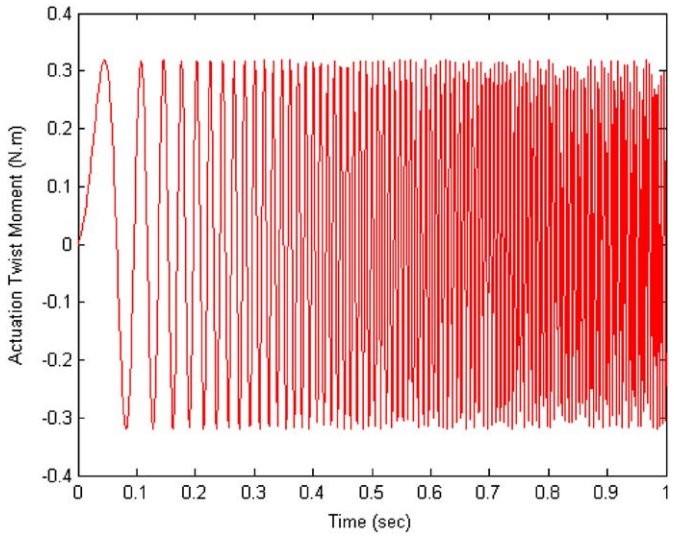

Fig. 17. Active input of twist moment.

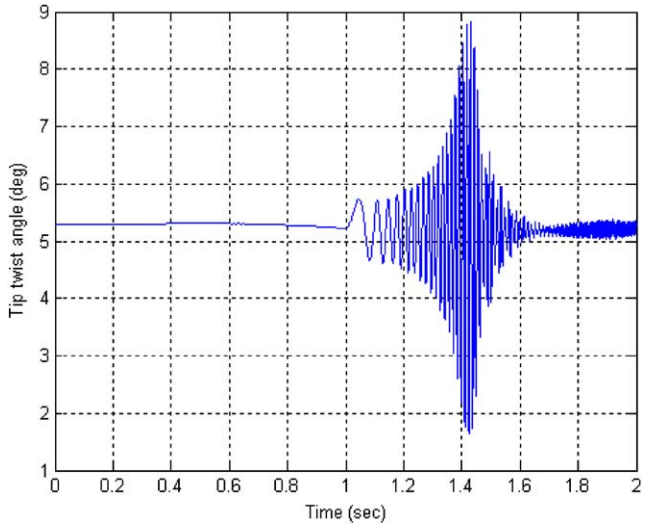

Fig. 18. Time history of tip twist angle in hover by a sine sweep actuation after 1 s.

FFT of the time response is presented in Fig. 19. The resonant peak is captured around 76 Hz, which compares well with the measured 74 Hz reasonance. The resonance magnitude, however, is approximately three times higher than the one obtained experimentally. This indicates that the aerodynamic damping is not being correctly capture, since this is the only source of damping in this analysis. Further investigation is necessary to determined the origin of the underestimation of the aerodynamic damping.

7. Concluding remarks

An overview of a new active aeroelastic aeroacoustic code has been presented. It couples a particle-wake panel code with an active nonlinear mixed variational intrinsic beam element code. An FW-H acoustic component has been

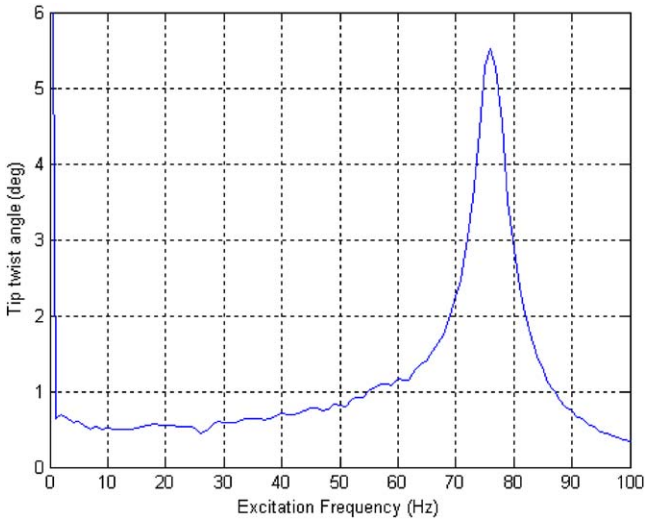

Fig. 19. Tip twist amplitude response of the ATR prototype blade in hover.

developed for inclusion in the new formulation. Preliminary acoustic and aeroelastic results were presented to demonstrate different aspects of the proposed formulation. While still further validation studies must be conducted, most of the results show good correlation with previously published data. The new capabilities of the complete code will provide rotorcraft structural dynamic, aerodynamic, acoustic, and active twist control studies within an integrated aeroelastic framework. Of particular importance, it will enable simultaneous noise and vibration studies of active twist rotor systems.

Acknowledgements

The second and third authors gratefully acknowledge the Natural Sciences and Engineering Research Council of Canada (NSERC) and the National Research Council of Canada (NRC) for partially supporting this effort. The usage of GENUVP 3.0 in this effort was possible through the research collaboration between the National Technical University of Athens and Carleton University. Technical discussions with Prof. Spyros Voutsinas (NTUA) are greatly appreciated.

References

Ahmed, S.R., Vidjaja, V.T., 1994. Unsteady panel method calculation of pressure distribution on BO105 model rotor blades and validation with DNW test data. Proceedings of the American Helicopter Society 50th Annual Forum, Washington, DC, pp. 1211–1231.

Anderson, C., 1986. A method of local corrections for computing the velocity due to a distribution of vortex blobs. Journal of Computational Physics 62, 111–123.

Beale, J.T., Majda, A., 1985. High order accurate vortex methods with explicit velocity kernels. Journal of Computational Physics 58, 188–208.

Beamier, P., Chelli E., Pahlke K., 2000. Navier–Stokes prediction of helicopter rotor performance in hover including aero-elastic effects. Proceedings of the American Helicopter Society 56th Annual Forum, Virginia Beach, Virginia, USA, pp. 391–401.

Bent, A.A., Hagood, H.W., 1997. Piezoelectric fiber composites with interdigitated electrodes. Journal of Intelligent Material Systems and Structures 8, 903–919.

Brentner, K.S., 1986. Prediction of helicopter rotor discrete frequency noise—a computer program incorporating realistic blade motions and advanced acoustic formulation. NASA TM No. 87721, NASA Langley Research Center, Hampton, Virginia, USA.

Cesnik, C.E.S., Shin, S.-J., 2001. On the modelling of active helicopter blades. International Journal of Solids and Structures. 38 (10–13), 1765–1789.

Cesnik, C.E.S., Shin, S.-J., Wilkie, W.K., Wilbur, M.L., 1999. Modelling, design, and testing of the NASA/Army/MIT active twist rotor prototype blade. Proceedings of the American Helicopter Society 55th Annual Forum, Montréal, Canada.

Cesnik, C.E.S., Shin, S.-J., Wilbur, M.L., 2001. Dynamic response of active twist rotor blades. Smart Materials and Structures 10, 62–76.

Cheng, T., 2002. Structural dynamics modelling of helicopter blades for computational aeroelasticity. Master's of Science Dissertation, Massachusetts Institute of Technology, Cambridge, MA, USA.

Conner, D.A., Hoad, D.R., 1982. Reduction of high-speed impulsive noise by blade planform modification of a model helicopter rotor. NASA TM No. 84553, NASA Langley Research Center, Hampton, VA, USA.

Farassat, F., Succi,, G.P, 1980. A review of propeller discrete frequency noise prediction technology with emphasis on two current methods for time domain calculations. Journal of Sound and Vibration 71 (3), 399–419.

Farassat, F., Succi, G.P., 1983. The prediction of helicopter rotor discrete frequency noise. Vertica 7 (4), 309–320.

Ffowcs-Williams, J.E., Hawkings, D.L., 1969. Sound generation by turbulence and surfaces in arbitrary motion. Philosophical Transactions of the Royal Society Series A 264, 321–342.

Hess, J.L., 1972. Calculation of potential flow about arbitrary three-dimensional lifting bodies. McDonnell Douglas Report No. MDCJ5679-01.

Hess, J.L., Smith, A.M.O., 1968. Calculation of non-lifting potential flow about arbitrary three-dimensional bodies. McDonnell Douglas Report No. ES 40622.

Hockney, R.W., Eastwood, J.W., 1981. Computer Simulation Using Particles 1st Edition. McGraw-Hill, New York.

Hodges, D.H., 1990. Mixed variational formulation based on exact intrinsic equations for dynamics of moving beams. International Journal of Solids and Structures 26 (11), 1253–1273.

Johnson, W., 1998. Rotorcraft aerodynamics models for a comprehensive analysis. Proceedings of the American Helicopter Society 54th Annual Forum, Washington, DC, USA.

Kube, R., Splettstoesser, W.R., Wagner, W., Seelhorst, U., Yu, Y.H., Boutier, A., Micheli, F., and Mercker, E., 1994. Initial results from the higher harmonic control aeroacoustic rotor test (HART) in the German-Dutch wind tunnel. Proceedings of the AGARD FDP Symposium on Aerodynamics and Aeroacoustics of Rotorcraft, CP-552, Berlin, Germany, October 10–13.

Leishman, J.G., 2000. Principles of Helicopter Aerodynamics, 1st Edition. Cambridge University Press, Cambridge.

Pahlke, K., Chelli, E., 2000. Calculation of multibladed rotors in forward flight using 3D Navier–Stokes method. Proceedings of the 26th European Rotorcraft Forum, The Hague, Netherlands, Paper No. 48.

Prechtl, E.F., Hall, S.R., 2000. Design and implementation of a piezoelectric servo-flap actuation system for helicopter rotor individual blade control. AMSL Report #00-03, Active Materials and Structures Laboratory, Massachusetts Institute of Technology, Cambridge, MA, USA.

Rehbach, C., 1973. Calcul d'ecoulements autour d'ailes sans epaisseur avec nappes tourbillonnaires evolutives. Recherche Aerospatiale, No. 2, pp. 53–61.

Shang, X., 1995. Aeroelastic stability of composite hingeless rotors with finite-state unsteady aerodynamics. Ph.D. Dissertation, Georgia Institute of Technology, Atlanta, GA, USA.

Shin, S.-J., 2001. Integral twist actuation of helicopter rotor blades for vibration reduction. Ph.D. Dissertation, Massachusetts Institute of Technology, Cambridge, MA, USA.

Splettstoesser, W.R., Junker, B., Schultz, K.-J., Wagner, W., Weitemeyer, W., Protopsaltis, A.,Fertis, D., 1993. The HELINOISE aeroacoustic rotor test in the DNW—test documentation and representative results. Report DLR-Mitt.-93–09 Göttingen, Germany.

Strawn, R.C., Djomehri R. C., 2001. Computational modelling of hovering rotor and wake aerodynamics. Proceedings of the American Helicopter Society 57th Annual Forum, Washington, DC, USA, pp. 1723–1734.

Vassberg, J.C., 1997. A fast surface panel method capable of solving million-element problems. AIAA Paper 97-0168.

Voutsinas, S.G., 1990. A generalized unsteady vortex particle method for solving the unsteady flow around multi-component configurations. NTUA Internal Report, National Technical University of Athens, Athens, Greece.

Voutsinas, S.G., Triantos, D.G., 1999a. High-resolution aerodynamic analysis of full helicopter configurations. Proceedings of the 25th European Rotorcraft Forum, Rome, Italy, Paper C11.

Voutsinas, S.G., Triantos, D.G., 1999b. Aeroacoustics of full helicopter configurations using vortex particle flow approximations. Proceedings of the CEAS Forum on Aeroacoustics of Rotors and Propellers, Rome, Italy.

Voutsinas, S.G., Belessis, M.A., Rados, K.G., 1995. Investigation of the yawed operation of wind turbines by means of a vortex particle method. AGARD-CP-552 FDP Symposium on Aerodynamics and Aeroacoustics of Rotorcraft, Berlin, Germany, Paper 11.

Wachspress, D.A., Quackenbush, T.R., Boschitsch A. H., 2000. Rotorcraft interactional aerodynamics calculations with fast vortex/fast panel methods. Proceedings of the American Helicopter Society 56th Annual Forum, Virginia Beach, VA, USA, pp. 51–71.

Zimcik, D.G., Wickramasinghe, V.K., Yong, C., Nitzsche, F., 2002. Smart spring' concept for active vibration control in helicopters. Proceedings of the American Helicopter Society 58th Annual Forum, Montréal, Canada.